Repurposing FDA-Approved Drugs for Temozolomide-Resistant IDH1 Mutant Glioma Using High-Throughput Miniaturized Screening on Droplet Microarray Chip

Haijun Cui, Xueyuan Sun, Marcel Schilling, Christel Herold-Mende, Markus Reischl, Pavel A. Levkin,* Anna A. Popova,* and Şevin Turcan*

To address the challenge of drug resistance and limited treatment options for recurrent gliomas with IDH1 mutations, a highly miniaturized screening of 2208 FDA-approved drugs is conducted using a high-throughput droplet microarray (DMA) platform. Two patient-derived temozolomide-resistant tumorspheres harboring endogenous IDH1 mutations (IDH1^{mut}) are utilized. Screening identifies over 20 drugs, including verteporfin (VP), that significantly affected tumorsphere formation and viability. Proteomics analysis reveals that nuclear pore complex may be a potential VP target, suggesting a new mechanism of action independent of its known effects on YAP1. Knockdown experiments exclude YAP1 as a drug target in tumorspheres. Pathway analysis shows that NUP107 is a potential upstream regulator associated with VP response. Analysis of publicly available genomic datasets shows a significant correlation between high NUP107 expression and decreased survival in IDH1^{mut} astrocytoma, suggesting NUP107 may be a potential biomarker for VP response. This study demonstrates a miniaturized approach for cost-effective drug repurposing using 3D glioma models and identifies nuclear pore complex as a potential target for drug development. The findings provide preclinical evidence to support in vivo and clinical studies of VP and other identified compounds to treat IDH1^{mut} gliomas, which may ultimately improve clinical outcomes for patients with this challenging disease.

1. Introduction

Adult diffuse gliomas are classified into three types: glioblastoma (GBM), oligodendroglioma, and astrocytoma.[1] Both oligodendroglioma and astrocytoma are defined by the presence of mutations in the isocitrate dehydrogenase (IDH) genes, IDH1 and IDH2.[1–4] These tumors are mostly diagnosed in younger patients, with a peak incidence in the third decade of life.[5–7] IDH mutation status is a strong predictor of both overall survival and treatment response and is routinely used to guide clinical decision making in the management of gliomas.[8,9] The majority of IDH mutations affect the metabolic enzyme IDH1, which catalyzes the conversion of isocitrate to α-ketoglutarate in the tricarboxylic acid (TCA) cycle.[10] In IDH1 mutant (IDH1^{mut}) gliomas, a single copy of the gene is mutated, resulting in the enzyme's new ability to catalyze the NADPH-dependent reduction of α-ketoglutarate to 2-Hydroxyglutarate,[10] which induces epigenetic and transcriptomic alterations.[4,11,12] Standard of care for glioma patients

H. Cui, P. A. Levkin, A. A. Popova
Institute of Biological and Chemical Systems – Functional Molecular Systems (IBCS-FMS)
Karlsruhe Institute of Technology (KIT)
Hermann-von-Helmholtz-Platz 1
76344 Eggenstein-Leopoldshafen, Germany
E-mail: pavel.levkin@kit.edu; anna.popova@kit.edu

H. Cui
Key Laboratory of Biorheological Science and Technology
Ministry of Education
College of Bioengineering
Chongqing University
Chongqing 400044, China

X. Sun, C. Herold-Mende, Ş. Turcan
Neurology Clinic and National Center for Tumor Diseases
University Hospital Heidelberg
Im Neuenheimer Feld 400, 69120 Heidelberg, Germany
E-mail: sevin.turcan@med.uni-heidelberg.de

M. Schilling, M. Reischl
Institute for Automation and Applied Informatics (IAI)
Karlsruhe Institute of Technology (KIT)
Hermann-von-Helmholtz-Platz 1
76344 Eggenstein-Leopoldshafen, Germany
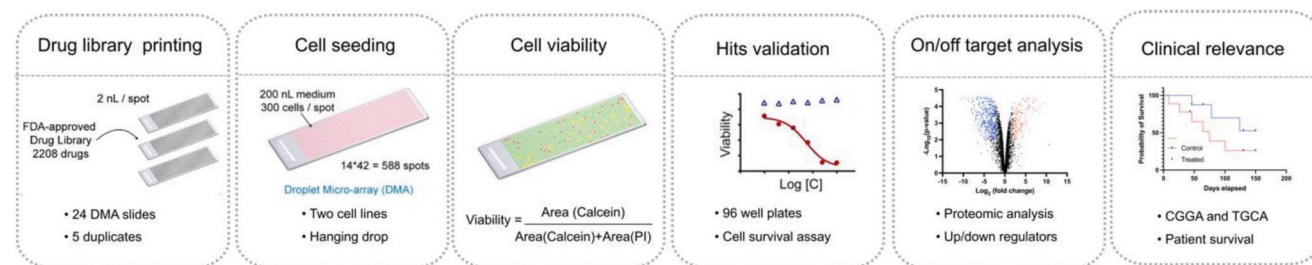
Scheme 1. Workflow for high-throughput drug screening and hit validation. The droplet microarray chip uses minimal reagents (200 nL medium, 300 cells per spot) to screen 2208 FDA-approved drugs rapidly and economically. The assay is validated using MTT assays in a standard 96-well plate. On- and off-target effects are assessed using Western blot and mass spectrometry. Drug target analysis is correlated with patient survival data from the Cancer Genome Atlas (TCGA) and the Chinese Glioma Genome Atlas (CGGA) databases to facilitate personalized clinical treatment.

includes surgery, radiation, and chemotherapy with either procarbazine, lomustine (CCNU), vincristine (PCV), or temozolomide (TMZ); however, IDH1^{mut} gliomas progress regardless of clinical treatment, and salvage options for progressive disease are limited.[13] Therefore, alternative effective therapeutic agents are urgently needed for glioma patients to extend overall survival and improve quality of life.[14,15]

To date, drug discovery efforts for IDH1^{mut} gliomas have been limited due to the paucity of preclinical models. Primary IDH1^{mut} patient-derived tumorspheres (PDTs) are challenging to culture in vitro, and even if successful, IDH1 mutation may be lost during cell culture.[16] As a result, PDTs derived from IDH1^{mut} tumors are rare, and they grow relatively slowly, making it difficult to obtain enough material for experiments requiring a large number of cells. This poses a significant challenge to drug screening efforts for IDH1^{mut} gliomas. Most studies have thus focused on drug discovery in GBMs.[17] However, given the limited treatment options and research tools, there is a need to develop appropriate in vitro screening platforms for IDH1^{mut} gliomas that enable the screening of a large number of compounds in physiologically relevant cell culture models with low cell requirements.

Our recently developed miniaturized Droplet Microarray (DMA) platform provides a solution for highly miniaturized high-throughput cell-based screening.[18–23] The DMA platform is a miniaturized chip with hundreds of nanoliter droplets, where the droplet volume depends on the size of hydrophilic spots surrounded by superhydrophobic barriers. These droplets can be used for independent 2D or 3D cell culture experiments, and due to their small volumes, the DMA can greatly reduce the consumption of cells, drugs, and reagents needed for the experiment.

In this study, we aimed to investigate the effectiveness of the DMA platform in identifying potential drug candidates for treating IDH1^{mut} gliomas (**Scheme 1**). We utilized the DMA chip to screen 2208 FDA-approved drugs against two IDH1^{mut} glioma PDTs. To create a single-spheroid array on DMA, we used the hanging drop method. The 3D cell spheroids were then subjected to high-throughput drug screening. We established an image analysis method based on live/dead fluorescence staining of

spheroids to discover potential drug candidates capable of preventing the formation and survival of 3D spheroids. The high-throughput screening resulted in the identification of more than 20 drugs that demonstrated efficacy as inhibitors of IDH1^{mut} PDT survival. We selected ten drugs for further validation, confirming their efficacy in our cell culture models. One of the drug candidates, verteporfin (VP), was selected for further investigation of its mechanism of action. Total lysate-mass spectrometry (MS) and functional assays revealed that VP was effective in killing IDH1^{mut} PDTs, potentially by disrupting the nuclear pore complex, independent of its known function as a YAP1 inhibitor. Thus, we have successfully established a workflow for miniaturized high-throughput screening of IDH1^{mut} PDTs on a DMA chip and identified potential drug candidates for further investigation (Scheme 1). Additionally, our mechanistic study on VP highlights the potential importance of nucleoporin studies in IDH1^{mut} gliomas.

2. Results and Discussion

2.1. Identification of TMZ-Resistant IDH1^{mut} PDTs

We utilized PDTs isolated from surgical/biopsy material of patients diagnosed with oligodendroglioma (TS603, SU-AO3, NCH612) and astrocytoma (NCH1681) (Table S1, Supporting Information). Tumorspheresderived from all four cell lines grew as suspensions and formed spheroid-like cell aggregates in uncoated cell culture flasks. We confirmed the presence of the IDH1 R132Hhotspot mutation in PDTs using Western blotting (**Figure 1**A). Compared with GBM PDTs, IDH1^{mut} cells exhibited slower growth rates (Figure S1A, Supporting Information). Next, we tested the response of the PDTs to TMZ using colorimetric-based MTT cell viability assay, which measures the metabolic activity of the cells. To establish a TMZ concentration gradient, we seeded an equal number of cells in 100 µL of medium into each well of a 96-well plate. The following day, we added 50 µL of medium containing varying amount of TMZ from the 97.2 mᴍ TMZ stock to each well to achieve the desired final concentration. After 96 h of incubation, we measured MTT readings and adjusted them by subtracting the background reading obtained from wells containing only medium but without cells. We then normalized the survival percentage of each treatment well to that of the non-TMZ treated wells based on the adjusted reading.

P. A. Levkin
Institute of Organic Chemistry (IOC)
Karlsruhe Institute of Technology (KIT)
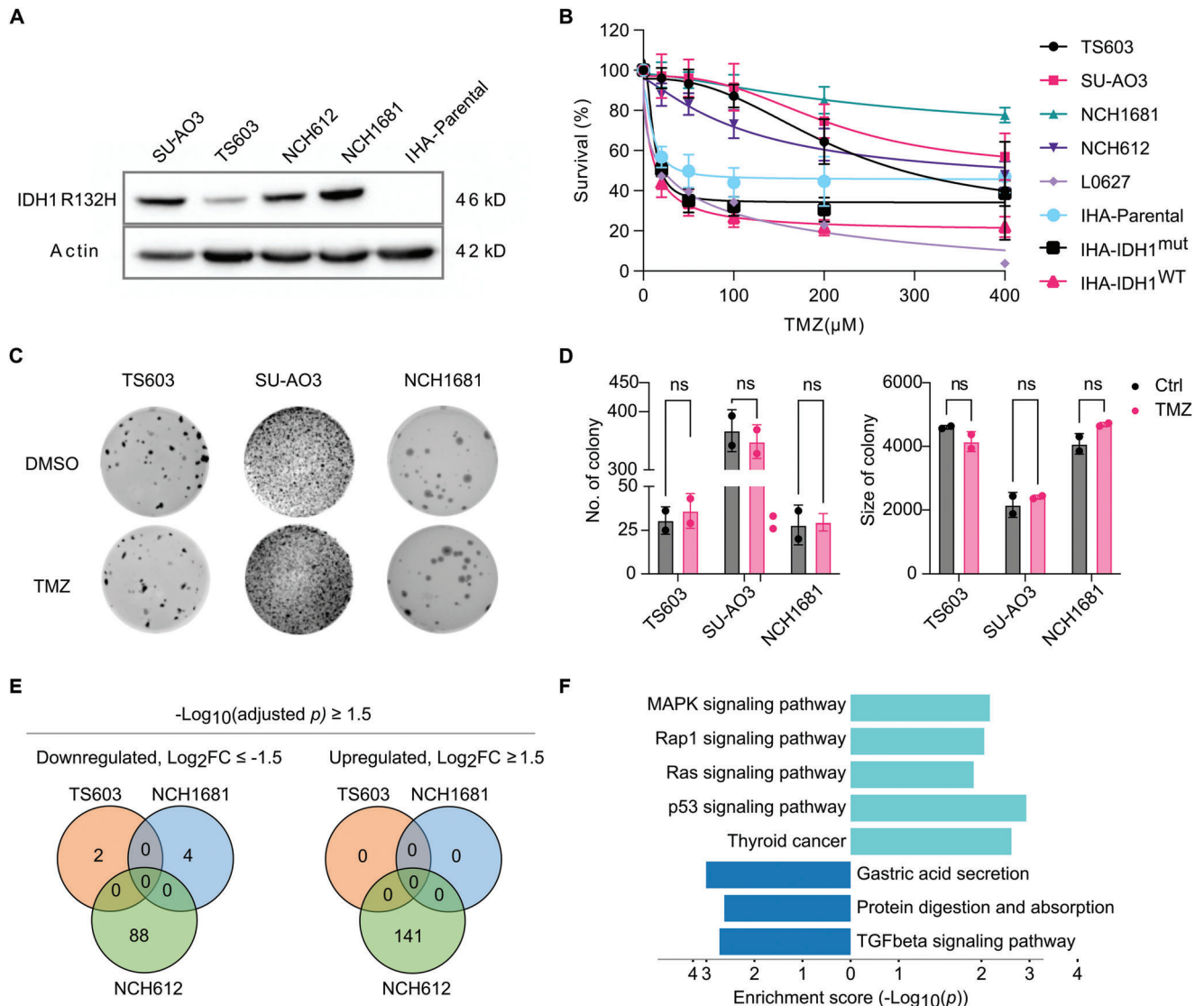Fritz-Haber Weg 6
76131 Karlsruhe, Germany

**ADVANCED
SCIENCE NEWS**

www.advancedsciencenews.com

**ADVANCED
HEALTHCARE
MATERIALS**

www.advhealthmat.de

Figure 1. Identification of TMZ-resistant IDH1^{mut} PDTs. A) Western blot confirms IDH1^{mut} protein expression in four PDTs. B) MTT viability assay shows IDH1^{mut} PDTs are more resistant to TMZ compared to IDH1^{WT} PDTs and IHAs ($n \geq 3$ biological repeats, each with three technical repeats). IC$_{50}$ calculations were made in GraphPad Prism with [inhibitor] vs. response (four parameter). C) The soft agar assay with daily treatment of 100 μM TMZ for 4 days, followed by one month of colony growth, indicates that TS603, SU-AO3, and NCH1681 cells are not responsive to TMZ treatment. 10 000 cells of TS603 and NCH1681, 15 000 of SU-AO3 were seeded. D) Colony number and size comparison using ImageJ analysis reveals no significant differences in colony number between TMZ and DMSO treatment in TS603, SU-AO3, and NCH1681. Unpaired two tailed t test was performed. E) Venn diagrams demonstrating the overlap of TMZ-driven translational changes with $-$Log$_{10}$ (adjusted p) ≥ 1.5, Log$_2$(fold change ≤ -1.5 and Log$_2$(fold change ≥ 1.5 in the 3 IDH1^{mut} PDTs. (F) KEGG pathway analysis of down- and up-regulated proteins in NCH612. Pathway analysis were done using Metascape and plotted using SRplot.

The IC$_{50}$ values were calculated using the GraphPad Prism software, based on the [inhibitor] vs response variable slope (four parameter) equation derived from the dose–response curve. The results showed that all IDH^{mut} PDTs exhibited a significantly higher IC$_{50}$ compared to GBM PDT and immortalized human astrocytes (IHAs) (Figure 1B; Table S1, Supporting Information). IHAs and isogenic cells expressing mutant IDH1 (R132H), wild-type IDH1, or neither were well-characterized and used in our previous studies to investigate the role of mutant IDH1 in gliomas.[4] Specifically, the IC$_{50}$ values for the IDH1^{mut} gliomas TS603, SU-AO3, NCH1681, and NCH612 were 211.3,

205.2, 252.2, and 121.5 μM, respectively. The IDH1^{WT} glioma line L0627 had an IC$_{50}$ of 71.75 μM, while the parental, IDH1^{mut} and IDH1^{WT} immortalized human astrocytes (IHAs) had IC$_{50}$ values of 10.61, 10.61, and 11.76 μM respectively. It is worth noting that all IDH1^{mut} PDTs had an IC$_{50}$ greater than 100 μM which is the upper limit for in vitro treatment with TMZ[24] due to its low clinically relevant dosages,[25] low solubility in DMSO, and sensitivity of cells to DMSO (Figure S1B, Supporting Information). Therefore, we determined that these IDH1^{mut} PDTs are TMZ-resistant (TMZ-R) based on the MTT cell viability assay.

**ADVANCED
SCIENCE NEWS**

www.advancedsciencenews.com

**ADVANCED
HEALTHCARE
MATERIALS**

www.advhealthmat.de

To further investigate the response of the PDTs to TMZ, we evaluated their anchorage-independent growth using a 3D soft agar culture system. This system involved seeding the cells in the middle layer of a three-layer agar culture, consisting of a top feeding layer, a middle cell layer, and a bottom supporting layer. After seeding 10 000–15 000 cells in the middle layer, we allowed the cells to recover for one week before treating them with 100 μM TMZ, which was administered continuously for four days with daily drug replacement. After 96 h, fresh drug-free medium was added, which was replenished weekly according to the cell growth rate. Approximately one month later, the colonies became visible to the naked eye, at which point they were stained with 0.005% crystal violet, and images were captured. Colony number and size were quantified with ImageJ. As shown (Figure 1C,D), there was no difference in colony number and size between 0.1% DMSO control and 100 μM TMZ-treated samples, indicating that TMZ does not affect the tumorigenic potential of IDH1^{mut} PDTs. Thus, we further confirmed the TMZ resistance (TMZ-R) of the three IDH1^{mut} PDTs - TS603, NCH1681, and SU-AO3. However, NCH612 displayed slightly higher sensitivity to TMZ compared with the other three IDH1^{mut} PDTs, as observed by direct cell number counting after 96 h of 100 μM TMZ treatment (Figure S1C, Supporting Information). For this experiment, cells were seeded in six-well laminin coated plates to facilitate adherence to the bottom of the plates for easier medium and drug change. A total of 1×10^5 cells of TS603, NCH1681, and NCH612, and 2×10^5 cells of SU-AO3 were seeded in a six-well plate. After the cells adhered to the plate the following day, 100 μM TMZ or 0.1% DMSO was added, and the TMZ was refreshed daily in 3 mL medium. After 4 days of drug treatment, cells were harvested and counted using trypan blue staining with an automated cell counter. In comparison to the 0.1% DMSO control, NCH612 had lower survival, while TS603, SU-AO3, and NCH1681 showed no survival difference between TMZ and DMSO control (Figure S1C, Supporting Information). However, it remains unclear whether NCH612 is TMZ-sensitive or not, as the previous MTT assay exhibited an IC$_{50}$ above 100 μM. Therefore, we aimed to investigate the transcriptional changes in the IDH1^{mut} PDTs upon TMZ treatment. We treated TS603, NCH1681 and NCH612 cells with 100 μM TMZ for 96 h with daily drug refreshing and performed RNA-seq analysis. Among the 16041 genes measured, genes with Log$_{10}$(adjusted p) > 1.5 were considered significant. We considered Log$_2$(fold change) ≤ −1.5 as downregulated and Log$_2$(fold change) ≥1.5 as upregulated. Our results indicated that only two genes were altered in TS603 and four genes were altered in NCH1681, indicating that their transcriptomes remained stable during TMZ treatment (Figure 1E; Figure S1D,E, Supporting Information). However, NCH612 exhibited transcriptional alterations upon TMZ treatment, with 88 downregulated and 141 upregulated genes, demonstrating slight TMZ sensitivity compared with the other two PDT lines (Figure 1E; Figure S1F, Supporting Information).

To explore the altered pathways, we submitted the 88 downregulated and 141 upregulated genes in NCH612 for Kyoto Encyclopedia of Genes and Genomes (KEGG) pathway analysis. We selected the KEGG pathways with $-\text{Log}_{10} p \geq 2$ from the database, and observed that the upregulated pathways showed high enrichment of p53, MAPK, Rap1, and Ras signaling pathways. The downregulated pathways were enriched for gastric acid secre-

tion, protein digestion and absorption, and TGF-β signaling pathway (Figure 1F). These findings suggest that although all four IDH1^{mut} PDTs display resistance to TMZ, the degree of transcriptional response varies among them. In summary, we employed a variety of assays, such as MTT viability, soft agar growth, cell number counting, and RNA-seq, to evaluate the TMZ-resistant phenotype of our IDH1^{mut} PDTs. Taken together, our results indicate that TS603, SU-AO3 and NCH1681 are resistant to TMZ and represent recurrent TMZ-R IDH1^{mut} PDTs.

2.2. 3D High-Throughput Miniaturized Drug Screening on the DMA Platform

To ensure the suitability of our DMA platform for high-throughput drug screening on TMZ-R IDH1^{mut} PDTs, we conducted initial experiments to validate the platform's ability to maintain 3D tumor growth and mimic the TMZ response in cultural wells. This section describes the results of these experiments and serves as the foundation for the subsequent high-throughput screening.

2.2.1. Recapitulation of 3D Tumor Growth and TMZ-R on the Miniaturized DMA

To recapitulate the 3D growth characteristics of PDTs, we utilized the hanging drop method to rebuild 3D cell spheroids on the DMA (**Figure 2**). The DMA used in this study had 588 square hydrophilic spots (1 mm × 1 mm), and each slide had a unique barcode to distinguish between different slides. Prior to cell seeding, we applied an anti-cell adhesion solution to the hydrophilic spots of DMA to reduce cell adhesion to the surface of the array (Figure 2A,B). Next, we printed 200 nL of culture medium containing 300 cells in the hydrophilic spots of DMA. Using the hanging drop method (culturing on DMA in inverted position), we obtained an array containing 588 independent single cell spheroids. Microscopy analysis showed that both NCH1681 and TS603 formed spheroids within 24 h of culture (Figure 2C,D). After 5 days of culture, the cell spheroids had diameters of 101.7 ± 9.3 μm and 105.4 ± 8.3 μm for NCH1681 and TS603 cells, respectively (Figure 2E,F). This indicates that both NCH1681 and TS603 lines can form 3D spheroids with uniform size and spherical shape on the DMA chip. Moreover, both spheroid lines exhibited resistance to TMZ in this miniaturized format similar to their response in the 96-well format (Figure 1B; Table S1, Supporting Information). Therefore, we successfully recapitulated the 3D growth and TMZ-R in nanoliter volumes on the DMA platform from IDH1^{mut} PDTs.

2.2.2. High-Throughput Screening Identifies Potential Candidates

To identify potential drugs for the treatment of TMZ-R IDH1^{mut} PDTs, we screened 2208 FDA-approved drugs at a concentration of 5 μM on NCH1681 and TS603 (Scheme 1, **Figure 3**). Before seeding the cells, we printed the drugs on the DMA as single agents in a specific order (Figure S2, Supporting Information). To determine the formation and viability of drug-treated tumor
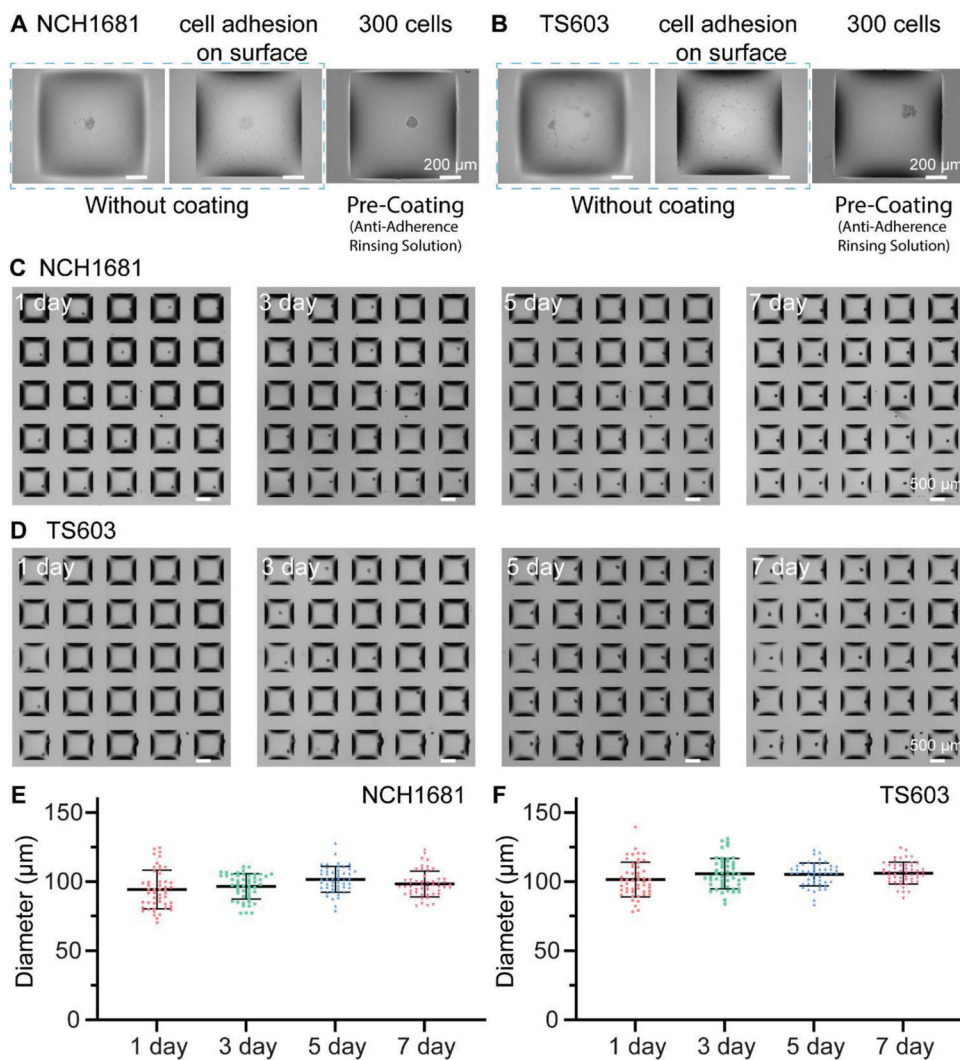
ADVANCED
SCIENCE NEWS

www.advancedsciencenews.com

ADVANCED
HEALTHCARE
MATERIALS

www.advhealthmat.de

Figure 2. Glioma spheroids on the DMA. A) Typical images of NCH1681 cultured in single droplet with and without an anti-cell adhesion coating. B) Typical images of TS603 cultured in single droplet with and without an anti-cell adhesion coating. C,D) The images of NCH1681 or TS603 spheroids after 1, 3, 5, and 7 days cultivation. The number of cells seeded is 300 cells per droplet, and the size of the spot is 1 mm × 1 mm. E,F) Plot of the spheroid diameter of NCH1681 or TS603 over time ($n = 50$).

spheres, we stained the spheroids with Calcein AM to label live cells and propidium iodide (PI) fluorescent staining to label dead cells. Using an automated microscope, we imaged all the spheroids on the DMA. To efficiently interpret the large amount of imaging data obtained, we developed a deep learning approach to obtain accurate segmentation of fluorescence images[26] (Figure S3, Supporting Information). We quantified the percent viability of each drug-treated spheroid compared to the viability of DMSO-treated spheroids and averaged the percent viability data in five replicates (Figure 3A; Figures S3 and S4, Supporting Information). We considered drugs that reduced viability to less than 50% compared to DMSO control as effective compound candidates. Based on this criterion, we identified 22 hits for TS603 and 29 hits for NCH1681, with ten hits shared between the two PDTs (Figure 3B).

To test the generality of the drug candidates and exclude any cell-specific results, we included NCH612 and SU-AO3 and

tested whether the candidate compounds induced cell killing using MTT assay in a 96-well format. Out of the ten drugs tested (Figure 3C; Table S2, Supporting Information), all PDTs showed sensitivity to the drugs with IC$_{50}$ below 1 µm. Overall, our study demonstrates the successful application of miniaturized high-throughput drug screening of 3D spheroid cultures on DMA. We identified over 20 potential drug candidates for each tested PDTs, representing a significant step toward the development of effective treatments for TMZ-R IDH^{mut} glioma.

2.3. Verteporfin as a Potential Therapeutic Target for IDH Mutant Gliomas

Verteporfin (VP) was selected for further assessment among the screened candidates due to its ability to cross the blood-brain barrier (BBB)[27,28] and its involvement in clinical trials for
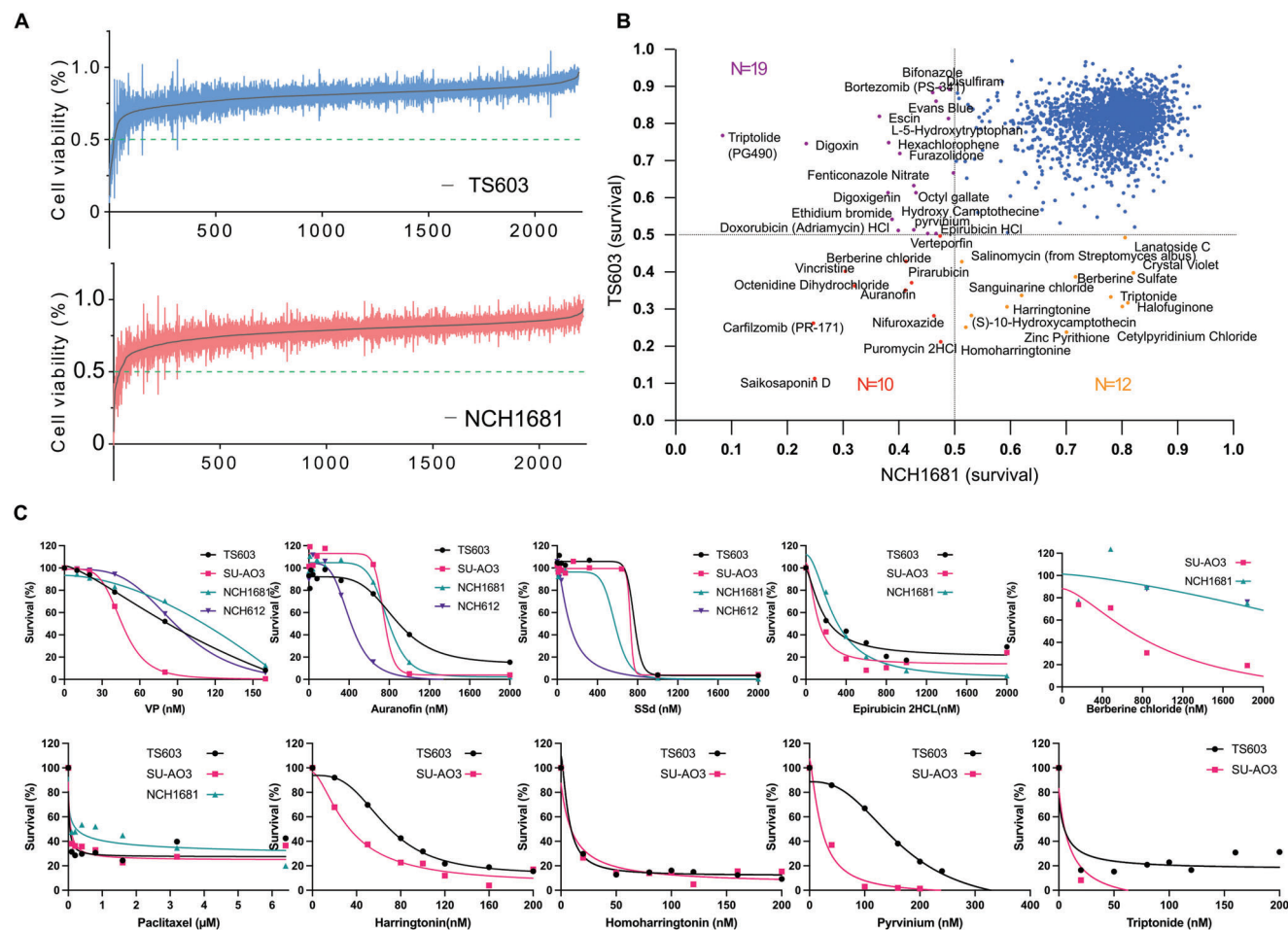
Figure 3. Identification and validation of drug candidates through high-throughput screening. A) Viability of TS603 and NCH1681 treated with drug library hit compounds. Positive hits were defined as those that resulted in over 50% inhibition of spheroid viability. B) Based on the criteria, 22 hits were identified in TS603 and 29 hits in NCH1681, with 10 hits shared between the two PDTs. Each dot on the graph represents a drug, with x-axis showing cell survival in NCH1681 and y-axis showing cell survival in TS603, demonstrating the drug efficacy in each cell line and both. C) The top candidates were further validated with MTT assay using a range of drug concentrations, which were narrowed down to the concentration gradient shown. For this assay, 1000 cells were seeded, and drug treatment lasted for 96 h, with each dot representing the average of three technical repeats.

treating GBMs.[27–30] We further confirmed VP's anti-tumor efficacy in TS603, NCH1681 and SU-AO3 using CellTiterGlo viability (Figure S5A, Supporting Information) and soft agar colony formation assays (Figure S5B, Supporting Information). VP is FDA-approved for the treatment of macular degeneration and has been reported to be a YAP1 (Yes1 Associated Transcriptional Regulator) inhibitor in many cancer types.[31,32] Therefore, we investigated whether VP inhibited YAP1 in our tumor models.

2.3.1. VP Exerts its Anti-Tumor Activity in IDH1^{mut} PDTs Independent of YAP1

The transcriptional regulator YAP1 has been implicated in cancer initiation and growth.[33] To investigate the role of YAP1 in the anti-tumor activity of VP in our PDTs, we conducted Western blot analysis and observed a time- and dose-dependent decrease in YAP1 protein levels following VP treatment in NCH1681 and TS603 cells (Figure S5C, Supporting Information). We found that

the PDTs exhibited different levels of endogenous YAP1 protein, with NCH1681 having the highest levels (**Figure** 4A). However, NCH1681 did not exhibit the strongest response to VP treatment, while SU-AO3, which has undetectable YAP1 levels, displayed higher sensitivity to VP exposure (Figure 4A; Table S2, Supporting Information). This negative correlation between YAP1 protein levels and IC$_{50}$ of PDTs to VP suggests that YAP1 may not be the only target of VP (Figure 4B). To test this hypothesis, we employed shRNA-mediated knockdown of YAP1 in both TS603 and NCH1681. The two shRNAs resulted in 90% and 50% knockdown in TS603 (Figure 4C) and 80% and 50% knockdown in NCH1681 (Figure 4E), respectively. Surprisingly, YAP1 loss did not affect the colony formation ability of TS603 (Figure S5D,E, Supporting Information), and cells with or without YAP1 maintained their sensitivity to VP treatment (data not shown). However, we observed that the greatest reduction in YAP1 level led to increased sensitivity to VP treatment(Figure 4D,F). For example, in TS603, shYAP1 1# with 90% of YAP1 knockdown showed a lower survival percentage to VP at 40 and 80 nM for 96 h
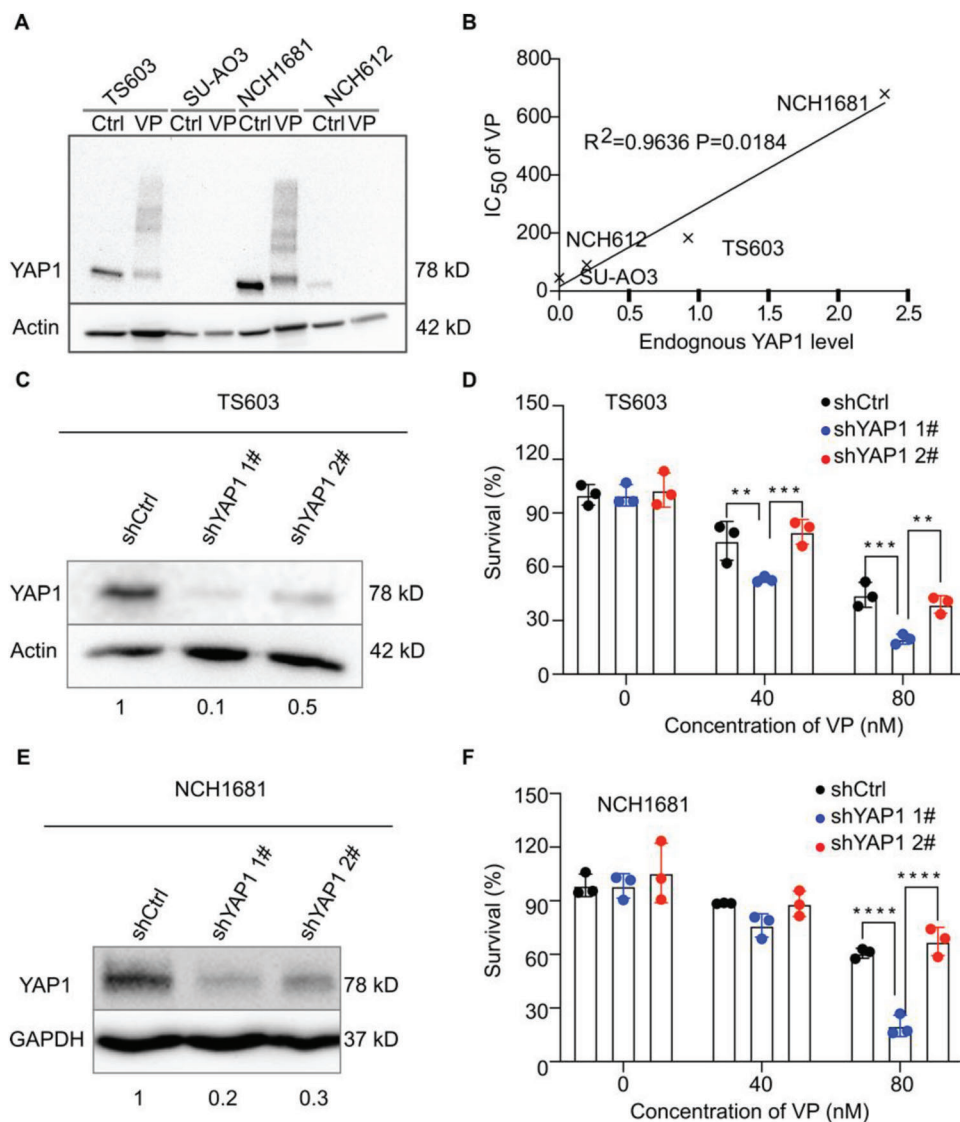
Figure 4. VP inhibits proliferation of IDH1^{mut} gliomas independently of YAP1. A) Endogenous YAP1 protein levels vary between IDH1^{mut} PDTs. B) Negative correlation between endogenous YAP1 protein levels and IC$_{50}$ of VP (shown in Table S1, Supporting Information) in PDTs. The endogenous YAP1 level is normalized to actin as shown in the Western blot in (A). C) shRNA-mediated YAP1 knockdown decreases YAP1 protein levels in TS603 cell line. Quantification of YAP1 protein levels is shown below the image. D) TS603 with lower levels of YAP1 shows greater sensitivity to VP in the MTT assay ($n = 3$ technical repeats). E) shRNA-mediated YAP1 knockdown decreases YAP1 protein levels in the NCH1681 cell line. Quantification of YAP1 protein levels is shown below the image. (F) NCH1681 with lower YAP1 levels show greater sensitivity to VP in the MTT assay ($n = 3$ technical repeats). The data were analyzed using two-way ANOVA, $p < 0.001$.

treatment compared to shYAP1 2#, which had only 50% YAP1 knockdown. Similarly, in NCH1681, shYAP1 1# with 80% YAP1 knockdown showed higher sensitivity than shYAP1 2#, which had 50% YAP1 knockdown. These results supported the notion that YAP1 may not be the sole target of VP in our PDTs. Overall, our results suggest that VP exerts its mode of action through a YAP1-independent mechanism in IDH1^{mut} PDTs.

2.3.2. VP Targets the Nucleoporin Family

To identify the target of VP in TMZ-R IDH1^{mut} PDT models, we performed whole-cell lysate mass spectrometry (MS) anal-

ysis to examine the global effect of VP on the proteome. We treated TS603, NCH1681, and SU-AO3 with 1 μM VP for 2 h, a dose at which significant YAP1 reduction was observed by Western blot (Figure S5C, Supporting Information). In total, we measured 5964 proteins in each PDT. To identify differentially abundant proteins, we applied an absolute Log$_2$(fold change) cutoff of 2 and a $-$Log$_{10}$(adjusted p) threshold of 2. VP treatment resulted in significant changes in protein expression levels in all three PDTs. Specifically, 134 proteins were upregulated, and 477 proteins were downregulated in TS603 (Figure S6A, Supporting Information), 104 proteins were upregulated and 363 proteins were downregulated in SU-AO3 (Figure S6B, Supporting Information), and 92 proteins were upregulated and 372 proteins were
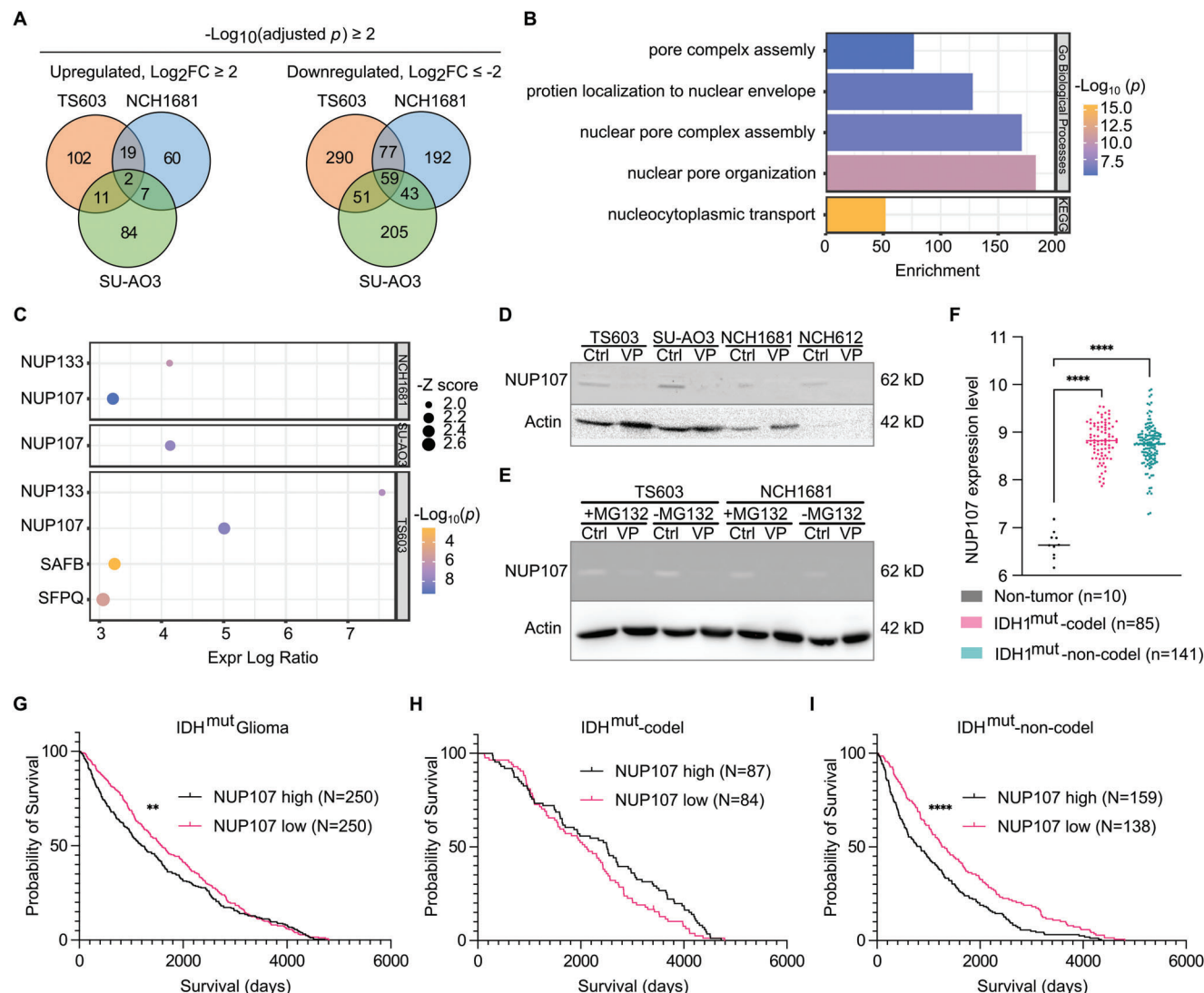
Figure 5. NUP107 as a response marker for VP in astrocytoma. A) Venn diagrams demonstrating the overlap of VP-driven translational changes (Log$_2$(fold change) ≤ -2 or ≥ 2 and $-$Log$_{10}$(adjusted p) ≥ 2) in the three IDH1^{mut} PDTs. B) GO and KEGG pathway analysis revealed nucleocytoplasmic transport as the commonly altered pathway among all tested PDTs, with a corresponding biological process involving the nuclear pore organization. C) IPA upstream pathway analysis predicted NUP107 as a regulator following VP treatment in all three tested PDTs. D) Western blot confirmed that NUP107 protein levels decreased upon 1 μM VP treatment for 1 h in all four tested PDTs. E) Proteasome inhibition using MG132 did not prevent NUP107 degradation upon VP treatment. F) Expression analysis of NUP107 gene obtained from TCGA data showed differential expression between non-tumors and IDH1^{mut} samples. Data analyzed with one-way ANOVA, $p < 0.0001$. G) Kaplan-Meier analysis showed that higher NUP107 expression correlated with shorter overall survival in IDH1^{mut} patients ($p = 0.0047$, Gehan-Breslow-Wilcoxon test). H) Kaplan-Meier analysis showed no difference in overall survival between high and low NUP107 expression in IDH1^{mut}-codel patients ($p = 0.0677$, Gehan-Breslow-Wilcoxon test). I) Kaplan-Meier analysis showed that higher NUP107 expression correlated with shorter overall survival in IDH1^{mut}-non-codel (astrocytoma) patients ($p < 0.0001$, Gehan-Breslow-Wilcoxon test).

downregulated in NCH1681 (Figure S6C, Supporting Information). Each PDT exhibited unique pathways for the up- and downregulated proteins, except for the decreased abundance of nucleocytoplasmic transport, which was commonly observed across all three PDTs (Figure S6D,F,H, Supporting Information).

After analyzing the proteins commonly altered in the three PDTs, we found that only two proteins were consistently upregulated across all lines, while 59 proteins were commonly downregulated (**Figure 5**A). These results suggest that VP treatment leads to a downregulation of the related pathways in all three IDH1^{mut}

PDTs. To explore the molecular networks, we submitted identified 59 proteins to Metascape for KEGG pathway and biological process analysis. Based on the $-$Log$_{10}$(p), Z score, gene hits and enrichment, we extracted the top KEGG pathway and biological process (Figure 5B). Our KEGG pathway analysis revealed a notable enrichment in the nucleocytoplasmic transport pathway, consistent with the previously analyzed shared pathways between the three PDTs when we conducted separate analyses for each PDT. The nuclear pore complex (NPC) was identified as the primary biological process affected by VP treatment (Figure 5B).

**ADVANCED
SCIENCE NEWS**

www.advancedsciencenews.com

**ADVANCED
HEALTHCARE
MATERIALS**

www.advhealthmat.de

NPCs play critical roles in the transportation of macromolecules between the nucleus and cytoplasm and are composed of around 30 nucleoporins (NUPs).[34,35] Upon further examination of the NUP family in our dataset, we observed that almost all NUP family members were significantly downregulated in all three PDTs (Figure S6E,G,I, Supporting Information), suggesting a specific impact of VP on this protein family.

To identify the upstream regulator responsible for the response to VP treatment in each PDT, we conducted an Ingenuity Pathway Analysis (IPA) , which predicted NUP107 to be a common upstream regulator (Figure 5C). To validate this prediction, we performed Western blot analysis and observed a significant reduction in NUP107 protein levels following VP treatment (Figure 5D). These findings suggest that NUP107 may play a crucial role in the response to VP treatment across multiple PDTs. To further understand the regulation of NUP107 , we tested whether it is degraded by the proteasome. However, treatment with MG132, a proteasome inhibitor, failed to rescue NUP107 protein degradation (Figure 5E). This suggests that NUP107 is degraded through a proteasome-independent pathway. Overall, our findings suggest that targeting the NUP family through VP treatment could be a promising therapeutic strategy for suppressing cell survival in IDH1^{mut} PDTs. Furthermore, the downregulation of NUPs highlights the potential importance of the NPCs in PDT survival and provides new insights into the development of targeted therapies for this tumor type.

2.3.3. High NUP107 Expression Correlates with Poor Patient Survival in Astrocytoma

We then investigated the clinical significance of NUP107 in IDH1^{mut} gliomas by examining whether its expression level correlated with grade or overall survival in two cancer genomic data platforms: The Cancer Genome Atlas (TCGA) and the Chinese Glioma Genome Atlas (CGGA). After analyzing the TCGA dataset, we found that NUP107 expression was significantly higher in IDH^{mut}-codel and IDH^{mut}-non-codel samples compared to normal tissues ($p < 0.0001$, ordinary one-way ANOVA), while there was no significant difference in NUP107 expression level between these two subtypes of IDH^{mut} glioma ($p = 0.3918$, ordinary one-way ANOVA) (Figure 5F). To gather sufficient data for survival analysis, we utilized the CGGA data set, which contained survival data from 500 patients with IDH mutant gliomas. Using the median Log_2 expression of NUP107 from IDH^{mut} glioma (3.2585) as a cut-off, we categorized patients as having high or low NUP107 expression. We found a significant difference in patient survival between those with high and low NUP107 expression (median overall survival of 1208 days for NUP107 high and 1582 days for NUP107 low; $p = 0.0047$, Gehan-Breslow-Wilcoxon test) (Figure 5G). Further analysis revealed no significant difference in survival in IDH^{mut}-codel patients (median overall survival of 2549 days for NUP107 high and 2097 days for NUP107 low; $P = 0.0677$, Gehan-Breslow-Wilcoxon test) (Figure 5H). However, in the group of IDH^{mut}-non-codel samples, we observed a significant difference in median overall survival between patients with high NUP107 expression (609 days) and those with low NUP107 expression (1286 days) ($p < 0.0001$, Gehan-Breslow-Wilcoxon test) (Figure 5I). This data

demonstrates that high NUP107 expression is associated with decreased overall survival in IDH^{mut} glioma, particularly in the IDH^{mut}-non-codel (astrocytoma) subtype. These results suggest that NUP107 expression level could potentially serve as a biomarker for predicting patient response to VP treatment.

3. Conclusion

In this study, we demonstrated the feasibility of building a 3D glioma spheroid model on the DMA chip for drug screening. We successfully identified over 20 FDA-approved drugs with therapeutic potential against TMZ-R IDH1^{mut} gliomas, which may provide urgently needed solutions for the clinical treatment of therapy resistant gliomas. We utilized two patient-derived IDH mutant glioma tumorspheres: TS603 (oligodendroglioma) and NCH1681 (astrocytoma), to construct a 3D cell spheroid model on DMA using the hanging drop method. Patient-derived gliomas typically grown as neurospheres in 3D cultures in stem-like conditions, which better recapitulate and more closely resemble the parental tumor. Therefore, these models are essential tools for translational research and offer benefits for in vivo and in vitro drug screening. This tool is especially important for study IDH1-mutant tumors, which are difficult, slow, and costly to culture in vitro.

Previously, we developed a Droplet Microarray (DMA) platform, which enables highly miniaturized high-throughput cell-based screenings in comparison to multiwell plates. This platform is based on hydrophilic–superhydrophobic patterning, and allows the formation of arrays of nanoliter droplets, each of which serves as a well for culturing and screening of cells. The DMA platform increases laboratory efficiency, dramatically reduces screening costs (by two to three orders of magnitude), and scales up the throughput (up to 30 times more wells per area). The DMA platform was demonstrated for formation of high-density single-spheroid-arrays, which are compatible with direct live microscopy-based characterizations. This tool offers a cost-effective and timely solution for patients, particularly for those who experience recurrence after standard treatment and have no available drug options. In the near future, we could obtain patient samples to conduct an FDA-approved drug screen to find the best drug or drug combination options for each individual. This approach can be integrated for the development of personalized medicine, enabling the identification of drugs tailored to each patient's needs.

Futhermore, we investigated the biological mechanism behind the killing effect of VP. Our findings suggest that nucleoporins, rather than YAP1, are the targets of VP, and we identified NUP107 as a predicted upstream regulator for VP response. Furthermore, CGGA data suggests that NUP107 may serve as a molecular marker for VP treatment and correlate with patient survival. Our study also highlights the potential of nucleopore complex (NPC) targeting as a novel pathway for the treatment of IDH1^{mut} gliomas. Our work provides a solid foundation for the future studies on drug repurposing in a cost-effective and efficient manner, as well as potential biomarkers to guide drug usage and inform clinical treatment decisions.

In summary, we have demonstrated a novel approach for identifying FDA-approved drugs with potential therapeutic benefits against TMZ-R IDH1^{mut} PDTs. Our miniaturized on-chip

**ADVANCED
SCIENCE NEWS**

www.advancedsciencenews.com

**ADVANCED
HEALTHCARE
MATERIALS**

www.advhealthmat.de

compound screening workflow enable us to screen a large number of drugs in a cost-effective and efficient manner. Through proteomic analysis, we investigated the mechanism of action of one of the identified drugs, verteporfin, and found that it targets the nuclear pore complex rather than the previously assumed target YAP1 in IDH1^{mut} PDTs. We further identified NUP107 as a potential biomarker for verteporfin treatment based on its association with patient survival in the CGGA database. Thus, the presented screening platform is optimal for studying rare diseases or cancers where tissue is sparse or not amenable to in vitro propagation (e.g., IDH^{mut} gliomas). Repurposing FDA approved drugs for glioma treatment using on-chip high-throughput drug screening with 3D spheroids shows great potential and lays the groundwork for future pharmaceutical interventions to assist tumor treatment in the clinic.

4. Experimental Section

Cell Lines and Cell Culture: Patient-derived IDH mutant glioma lines TS603, NCH1681, NCH612, SU-AO3 were maintained in Neurocult Basal Medium with proliferation supplements (Stemcell, Cat. # 05751), 20 ng mL^{-1} EGF (Stemcell, Cat. # 78006.2), 20 ng mL^{-1} basic-FGF (Stemcell, Cat. # 78003.2) and 2 µg mL^{-1} Heparin (StemCell, Cat. # 07980). HEK293TN and NHAs were maintained in DMEM-high glucose (Sigma, D5796) supplemented with 10% fetal bovine serum (Gibco, A476680). The patient-derived tumorspheres were obtained as follows: TS603 (oligodendroglioma) from Memorial Sloan Kettering Cancer Center; NCH612 (astrocytoma) and NCH1681 (astrocytoma) from Heidelberg University Hospital; SU-AO3 (oligodendroglioma) cells were kindly provided by Dr. Michelle Monje (Stanford University).

Preparation of 3D Glioma Spheroid Array: The cells were harvested and dissociated into single-cell suspension using Accutase (BioLegend, Inc. 423201). The droplet microarray (DMA) slides were purchased from Aquarray GmbH (catalog, IR0050241542, Eggenstein-Leopoldshafen, Germany). The DMA had 588 square hydrophilic spots (1 mm^2) and each slide had a unique barcode to distinguish between different slides. The spots of the DMA were coated with anti-adherence rinsing solution (50 nL, catalog # 07010, STEMCELL Technologies Inc.) and dried under sterile conditions. Then, using a universal liquid dispenser (I-DOT, Dispendix GmbH, Germany), 200 nL of cell suspension (cell concentration, 1.5×10^6 mL^{-1}) was dispensed to each spot. The DMA slide was immediately inverted and cultured in an incubator using the hanging drop method. For both tumorspheres, the spheroids were imaged after 1, 3, 5, and 7 days of cultivation using the microscope (Keyence BZ-X800, Japan).

High-Throughput FDA Compounds Screening on DMA: For high throughput screening, different drugs were printed in each spot of DMA in advance before printing the cells (Figure S2, Supporting Information). The FDA-approved drug library was purchased from Selleck Chemicals LLC and stored as required by suppliers (L1300-Z351463, https://www.selleckchem.com/screening/fda-approved-drug-library.html). The non-contact dispensing system (sciFLEXARRAYER, SCIENION AG. Germany) was used to print 2 nL of the drug solution in DMSO into each spot. The final drug concentration in droplets with cells was 5 µM and there were five replicates for each drug. Drugs (2208) were printed on total 24 DMA slides. The outer rows were not used for drug screening because of the edge effect. Each slide contained 92 drugs and 1 DMSO control group. The two tumorspheres (NCH1681, TS603) were then seeded on the DMA in an amount of 300 cells in 200 nL medium per each spot. The slides were incubated for 3 days using the hanging drop method. Afterward, cells were stained with Calcein AM (1/2000) and PI (1/2000) for 20 min. The DMA slide was imaged by automated screening microscope Leica Thunder 3D Imager (Leica Microsystems, Germany).

Analysis of Screening Results: Upon completion of high-throughput screening, the images were exported as TIF format (Figure S3, Supporting Information). Each spot had two channels, green and red, which represent live cells and dead cells respectively. A deep learning system was developed to obtain the accurate segmentation of fluorescence images. To distinguish non-cellular fluorescent signals and reduce background interference, a pre-labeling was used to optimize image processing. On this basis, the area of spheroids in green and red fluorescent channels was accurately obtained, representing live and dead parts of spheroids, respectively. The green area was set as Area (Calcein) and the red area as Area (PI). The viability of each spheroid was estimated as Area (Calcein) / [Area (Calcein)+Area (PI)].

MTT Assay: For cell survival analysis, 3000 cells in 100 µL medium were seeded in a 96 well plate. The next day, the drugs were diluted in 50 µL of medium with different concentrations and added into the well accordingly. Ten microliters of 10 mg mL^{-1} MTT (Sigma, Cat. # M5655) were added in the well after 96 h of drug treatment, after another 2 h of incubation at 37 °C, 100 µL of solvent (10% SDS in 0.01 M HCl) were added, and color was measured the next day with Microplate reader infinite 200Pro at 580 nm wavelength with the plate background of 670 nm wavelength. The intensity of the reading was converted into viability percentage from negative control, by normalizing the readings to the DMSO control. The following drugs were used for the MTT assay: Verteporfin (Sigma, SML0534-5mg), Paclitaxel (Sigma, T7191-1mg), Harringtonin (SCBT, sc-204771-5mg), Epirubicin hydrochloride (Merck, E9406-5mg), Triptonide (SCBT, sc-200122-1mg), Homoharringtonine (SCBT, sc-202652-1mg), Pyrvinium (Selleck, s5816-5mg), Auranofin (Selleck, S4307-5mg), Saikosaporin D (Selleck, S5454-1mg), Berberine Chloride (Selleck, S2271-10mg), Temozolomide (Sigma, T2577-25mg).

CellTiter-Glo Cell Viability Assay: This assay was performed according to the manufacturer recommendations (Promega, Cat. #G9241).

Soft Agar Anchorage-Independent Growth Assay: For anchorage-independent cell survival assay, 100 000 to 150 000 cells were seeded in 0.4% soft agar (Lonza, Cat. # 50101) in six-well plates between 0.6% (top) and 0.8% (bottom) agar, after 2 weeks of growth with fresh medium, 1 µM VP or 0.04% DMSO control were added to the media for 1 h treatment. After additional 4 weeks of culturing in fresh media, cells were stained with 0.005% crystal violet (Sigma, SML0534) and imaged using the Bio-Rad ChemiDoc XRS+ imaging system. The colonies were counted by eye or with ImageJ software. Soft agar assay for TMZ response: 10 000 cells from TS603 and NCH1681, 15 000 cells of SU-AO3 are seeded in 12 well plate, after 1 week of cell growth, 100 µM TMZ or 0.1% DMSO were refreshed daily refreshed continuously for four days, then images were taken after 0.005% crystal violet staining. One month later , colony number and size comparison between PDTs was analyzed with ImageJ; all colonies were having the same threshold with removal of background and particle size between 100 and 200. a

Western Blot: The cells were pelleted by centrifuging at 900 rpm for 5 min, washed with cold PBS three times, and lysed with 120 µL (per six well plate) M-PER Extraction reagents (ThermoFisher #78501) containing 1X Protease Inhibitor Cocktail (Roche, SKU11697498001). The lysates were sonicated with Sonorex Digitec (Bandelin) for 2 min, incubated on ice for 30 min, centrifuged at 13 000 g for 15 min at 4 °C, and the supernatant was collected in 1.5 mL microcentrifuge tubes. The protein concentration was measured with BCA Protein Assay Kit according to manufacturer's protocol (ThermoFisher, #23225). For western blotting, 20 µg of protein was loaded with 4X Laemmli Buffer (BioRad, #1610747) containing 10% β-mercaptoethanol (Sigma, #M6250) and boiled at 95 °C for 10 min. The lysates were run on 10% resolving and 5% stacking SDS-PAGE gels for the electrophoresis. The proteins were blotted on 0.2 µm PVDF membrane (Bio-Rad) using the Mini-PROTEAN Tetra electrophoresis wet blot system (Bio-Rad) for proteins with molecular weights (MW) > 100 kD or iBLot2 for MWs < 100 kD. The transfer efficacy was checked with Coomassie dye (Thermal fisher, #20279) gel staining and Ponceau Red (ThermoFisher, 46430) membrane staining. The membrane with Ponceau is washed with TBST and blocked for 1 h in 5% milk at 4 °C. Primary antibodies were applied overnight at 4 °C in 5% milk. Protein signal was detected using Pierce ECL Western Blotting Substrate (ThermoFisher, #32109) and ChemiDoc MP Gel Imaging System (Bio-Rad). To probe the same membrane, the membranes were stripped with Restore PLUS Western Blot-Stripping-Buffer (ThermoFisher, #46430) for 15 min twice, and washed with TBST

and re-blocked in 5% milk before the next immunoprobing experiment. The antibodies used for the immunoblots were anti-glyceraldehyde 3-phosphate dehydrogenase (GAPDH) (Cell Signaling, #2118), anti-beta actin (ACTB) (Cell Signaling, #4967) anti–IDH1 R132H (Dianova, #DIA-H09), and anti-ACTB (Sigma, #A3854), Alexa Fluor 647 anti-Nuclear Pore Complex Proteins Antibody (Biolegend, #682203).

Mass Spectrometry Analysis: Whole cell lysates from three replicates per condition (drugs and control) from 1×10^6 cells were prepared. Proteomics were performed at the Mass Spectrometry Core Facility at the German Cancer Center (DKFZ). Data analysis was carried out by MaxQuant. Identification FDR cutoffs were 0.01 on peptide level and 0.01 on protein level. For VP treatment LFQ and iBAQ values were normalized via variance stabilization normalization. The statistical analysis for LFQ- or respectively iBAQ values was performed with the R-package "limma". The p-values were adjusted with the Benjamini–Hochberg method for multiple testing.

Immunofluorescence and Microscopy: For immunofluorescence analysis, 12 mm coverslips were placed into 12-well dishes, and coated with 10 µg mL^{-1} laminin (Sigma, L2020-1MG) overnight at 4 °C. On the next day, the coverslips were washed three times with PBS. Cells (1×10^5) were seeded and treated with 1 µM VP or 0.04% DMSO in triplicate for 3 h the next day. After removing the drug, cells were washed with PBS and fixed with 4% PFA for 20 min at room temperature. PFA was removed and cells were washed twice using PBS. Cells were permeabilized using 0.1% of Triton X-100 for 15 min at room temperature, followed by three gentle washes using PBS. For VP subcellular observation 1 drop of anti-fade mounting medium containing DAPI (VECTASHIELD, H-1200-10) was dispensed onto the microscope slide. The coverslips were mounted with the cells facing toward the microscope slide. The image z-stacks acquisition of T-PMT (bright field), Alexa-405 (DAPI), and Alexa-633 (autofluorescence of VP) was performed with Zeiss LSM710 Confocal microscope, using 63x (oil) objective, all controlled by ZEISS ZEN microscope software.

Viral Transductions: YAP1 was knocked down in TS603 and NCH1681 tumorspheres by viral transduction using two shRNA plasmids (shYAP1 #1, Addgene #42540; shYAP1 #2, Addgene #42541), and scrambled control plasmid (pLKO.1 puro, Addgene #8453). For virus production, 2×10^5 HEK293TN cells were seeded in six-well plates, transfection mixtures (1 µg target Plasmid + 0.6 µg envelope plasmid (pCMV-VSV-G, Addgene #8454) + 0.6 µg packaging plasmid (psPAX2, Addgene #12260) + 6.6 µL FuGene (Promega, E2311) + OptiMEM media (Gibco, # 31985062) up to a total of 100 µL) were added the next day. Cell culture medium was changed after 24 hours and collected for harvesting at 48 and 72 hours after transfection and filtered through 0.45 µm filters. The filtered cell culture supernatant was mixed in 3:1 ratio to a lab-made filtered 4 x virus precipitation buffer (40 g PEG 8000, 7 g NaCl, 10 mL PBS, final pH adjusted to 7.4 with 1 M HCl, filled up to 100 mL with distilled water) and incubated overnight at 4 °C. Next, the PEG/medium mix was centrifuged at 1600 x g at 4 °C for 45 min for virus collection. Supernatant was discarded, virus pellets were resuspended in 250 µL PBS and added to the NCH1681 and TS603 tumorspheres (seeded with density of 3×10^5 cells per six well-plate one day ahead of transduction) 100 µL a time, and another 100 µL after 24 h. Transfection efficacy was checked 48 h post-transfection by imaging with fluorescence microscope and counting the number of fluorescent cells. Stably transduced cells were selected with fresh complete medium containing 0.5–1 µg mL^{-1} puromycin every 3 to 4 days until drug-resistant colonies become visible (generally 7–14 days after selection). As selection control, parental cells were used. HEK293-TN, NCH1681 and TS603 were passaged at least two times and less than ten times before transduction and after thawing from the liquid nitrogen stock.

Statistical Analysis: Student's t test and 1- or 2-way ANOVA were used, as appropriate, to calculate significance ($^*p < 0.05$, $^{**}p < 0.01$, $^{***}p < 0.001$) in cell culture and imaging studies.

Supporting Information

Supporting Information is available from the Wiley Online Library or from the author.

Conflict of Interest

The authors declare no conflict of interest.

Data Availability Statement

The data that support the findings of this study are available from the corresponding author upon reasonable request.

[1] A. M. Molinaro, J. W. Taylor, J. K. Wiencke, M. R. Wrensch, *Nat. Rev. Neurol.* **2019**, *15*, 405.

[2] J. Bi, S. Chowdhry, S. Wu, W. Zhang, K. Masui, P. S. Mischel, *Nat. Rev. Cancer* **2020**, *20*, 57.

[3] J. Huang, J. Yu, L. Tu, N. Huang, H. Li, Y. Luo, *Front Oncol* **2019**, *9*, 506.

[4] S. Turcan, D. Rohle, A. Goenka, L. A. Walsh, F. Fang, E. Yilmaz, C. Campos, A. W. M. Fabius, C. Lu, P. S. Ward, C. B. Thompson, A. Kaufman, O. Guryanova, R. Levine, A. Heguy, A. Viale, L. G. T. Morris, J. T. Huse, I. K. Mellinghoff, T. A. Chan, *Nature* **2012**, *483*, 479.

[5] T. Komori, *Lab Invest* **2022**, *102*, 126.

[6] M. Weller, M. van den Bent, M. Preusser, E. Le Rhun, J. C. Tonn, G. Minniti, M. Bendszus, C. Balana, O. Chinot, L. Dirven, P. French, M. E. Hegi, A. S. Jakola, M. Platten, P. Roth, R. Rudà, S. Short, M. Smits, M. J. B. Taphoorn, A. von Deimling, M. Westphal, R. Soffietti, G. Reifenberger, W. Wick, *Nat. Rev. Clin. Oncol.* **2021**, *18*, 170.

[7] T. Jiang, D.-H. Nam, Z. Ram, W.-s. Poon, J. Wang, D. Boldbaatar, Y. Mao, W. Ma, Q. Mao, Y. You, C. Jiang, X. Yang, C. Kang, X. Qiu, W. Li, S. Li, L. Chen, X. Li, Z. Liu, W. Wang, Y. Bai, Y. Yao, S. Li, A. Wu, K. Sai, G. Li, K. Yao, X. Wei, X. Liu, Z. Zhang, et al., *Cancer Lett.* **2021**, *499*, 60.

[8] K. J. Habashy, R. Mansour, C. Moussalem, R. Sawaya, M. J. Massaad, *Br. J. Cancer* **2022**, *127*, 976.

[9] K. Aldape, K. M. Brindle, L. Chesler, R. Chopra, A. Gajjar, M. R. Gilbert, N. Gottardo, D. H. Gutmann, D. Hargrave, E. C. Holland, D.

T. W. Jones, J. A. Joyce, P. Kearns, M. W. Kieran, I. K. Mellinghoff, M. Merchant, S. M. Pfister, S. M. Pollard, V. Ramaswamy, J. N. Rich, G. W. Robinson, D. H. Rowitch, J. H. Sampson, M. D. Taylor, P. Workman, R. J. Gilbertson, *Nat. Rev. Clin. Oncol.* **2019**, *16*, 509.

[10] L. Dang, D. W. White, S. Gross, B. D. Bennett, M. A. Bittinger, E. M. Driggers, V. R. Fantin, H. G. Jang, S. Jin, M. C. Keenan, K. M. Marks, R. M. Prins, P. S. Ward, K. E. Yen, L. M. Liau, J. D. Rabinowitz, L. C. Cantley, C. B. Thompson, M. G. Vander Heiden, S. M. Su, *Nature* **2009**, *462*, 739.

[11] D. Rohle, J. Popovici-Muller, N. Palaskas, S. Turcan, C. Grommes, C. Campos, J. Tsoi, O. Clark, B. Oldrini, E. Komisopoulou, K. Kunii, A. Pedraza, S. Schalm, L. Silverman, A. Miller, F. Wang, H. Yang, Y. Chen, A. Kernytsky, M. K. Rosenblum, W. Liu, S. A. Biller, S. M. Su, C. W. Brennan, T. A. Chan, T. G. Graeber, K. E. Yen, I. K. Mellinghoff, *Science* **2013**, *340*, 626.

[12] C. Lu, P. S. Ward, G. S. Kapoor, D. Rohle, S. Turcan, O. Abdel-Wahab, C. R. Edwards, R. Khanin, M. E. Figueroa, A. Melnick, K. E. Wellen, D. M. O'Rourke, S. L. Berger, T. A. Chan, R. L. Levine, I. K. Mellinghoff, C. B. Thompson, *Nature* **2012**, *483*, 474.

[13] J. J. Miller, F. Loebel, T. A. Juratli, S. S. Tummala, E. A. Williams, T. T. Batchelor, I. Arrillaga-Romany, D. P. Cahill, *Neuro Oncol* **2019**, *21*, 669.

[14] S. Kannan, A. K. Murugan, S. Balasubramanian, A. K. Munirajan, A. S. Alzahrani, *Biochem. Pharmacol.* **2022**, *201*, 115090.

[15] M. Touat, Y. Y. Li, A. N. Boynton, L. F. Spurr, J. B. Iorgulescu, C. L. Bohrson, I. Cortes-Ciriano, C. Birzu, J. E. Geduldig, K. Pelton, M. J. Lim-Fat, S. Pal, R. Ferrer-Luna, S. H. Ramkissoon, F. Dubois, C. Bellamy, N. Currimjee, J. Bonardi, K. Qian, P. Ho, S. Malinowski, L. Taquet, R. E. Jones, A. Shetty, K.-H. Chow, R. Sharaf, D. Pavlick, L. A. Albacker, N. Younan, C. Baldini, et al., *Nature* **2020**, *580*, 517.

[16] S. Piaskowski, M. Bienkowski, E. Stoczynska-Fidelus, R. Stawski, M. Sieruta, M. Szybka, W. Papierz, M. Wolanczyk, D. J. Jaskolski, P. P. Liberski, P. Rieske, *Br. J. Cancer* **2011**, *104*, 968.

[17] S. Lenin, E. Ponthier, K. G. Scheer, E. C. F. Yeo, M. N. Tea, L. M. Ebert, M. Oksdath Mansilla, S. Poonnoose, U. Baumgartner, B. W. Day, R. J. Ormsby, S. M. Pitson, G. A. Gomez, *Int. J. Mol. Sci.* **2021**, *22*, 4322.

[18] W. Lei, A. Deckers, C. Luchena, A. Popova, M. Reischl, N. Jung, S. Bräse, T. Schwartz, I. K. Krimmelbein, L. F. Tietze, P. A. Levkin, *Adv Biol* **2022**, *6*, 2200166.

[19] H. Cui, X. Wang, J. Wesslowski, T. Tronser, J. Rosenbauer, A. Schug, G. Davidson, A. A. Popova, P. A. Levkin, *Adv. Mater.* **2021**, *33*, 2006434.

[20] Y. Liu, T. Tronser, R. Peravali, M. Reischl, P. A. Levkin, *Adv. Biosyst.* **2020**, *4*, 1900257.

[21] A. A. Popova, T. Tronser, K. Demir, P. Haitz, K. Kuodyte, V. Starkuviene, P. Wajda, P. A. Levkin, *Small* **2019**, *15*, 1901299.

[22] M. Benz, M. R. Molla, A. Böser, A. Rosenfeld, P. A. Levkin, *Nat. Commun.* **2019**, *10*, 2879.

[23] A. A. Popova, D. Marcato, R. Peravali, I. Wehl, U. Schepers, P. A. Levkin, *Adv. Funct. Mater.* **2018**, *28*, 1703486.

[24] X. Sun, S. Turcan, *Cells* **2021**, *10*, 1225.

[25] J. Portnow, B. Badie, M. Chen, A. Liu, S. Blanchard, T. W. Synold, *Clin. Cancer Res.* **2009**, *15*, 7092.

[26] M. P. Schilling, L. Rettenberger, F. Münke, H. Cui, A. A. Popova, P. A. Levkin, R. Mikut, M. Reischl, *Proceedings–31. Workshop Computational Intelligence*, KIT Scientific Publishing, Berlin, Germany **2021**, 211.

[27] R. D. Read, *Neuro Oncol* **2022**, *24*, 708.

[28] A. M. Barrette, H. Ronk, T. Joshi, Z. Mussa, M. Mehrotra, A. Bouras, G. Nudelman, J. G. Jesu Raj, D. Bozec, W. Lam, J. Houldsworth, R. Yong, E. Zaslavsky, C. G. Hadjipanayis, M. R. Birtwistle, N. M. Tsankova, *Neuro Oncol* **2021**, *24*, 694.

[29] M.-E. Halatsch, R. E. Kast, G. Karpel-Massler, B. Mayer, O. Zolk, B. Schmitz, A. Scheuerle, L. Maier, L. Bullinger, R. Mayer-Steinacker, C. Schmidt, K. Zeiler, Z. Elshaer, P. Panther, B. Schmelzle, A. Hallmen, A. Dwucet, M. D. Siegelin, M.-A. Westhoff, K. Beckers, G. Bouche, T. Heiland, *Neuro-Oncol. Adv.* **2021**, *3*, vdab075.

[30] J. M. Madeira, E. Bajwa, M. J. Stuart, S. Hashioka, A. Klegeris, *J. Neuroimmunol.* **2014**, *276*, 71.

[31] H. Zhang, S. K. Ramakrishnan, D. Triner, D. Centofanti, D. Maitra, B. Győrffy, J. S. Sebolt-Leopold, M. K. Dame, J. Varani, D. E. Brenner, E. R. Fearon, M. B. Omary, Y. M. Shah, *Sci. Signaling* **2015**, *8*, ra98.

[32] D. M. Brown, P. K. Kaiser, M. Michels, G. Soubrane, J. S. Heier, R. Y. Kim, J. P. Sy, S. Schneider, *N. Engl. J. Med.* **2006**, *355*, 1432.

[33] F. Zanconato, M. Cordenonsi, S. Piccolo, *Cancer Cell* **2016**, *29*, 783.

[34] S. Sakuma, M. Raices, J. Borlido, V. Guglielmi, E. Y. S. Zhu, M. A. D'Angelo, *Cancer Discovery* **2021**, *11*, 176.

[35] S. Xu, M. A. Powers, *Semin Cell Dev Biol* **2009**, *20*, 620.